Navier-Stokes Computations of Vortical Flows Over Low-Aspect-Ratio Wings

James L. Thomas*
NASA Langley Research Center, Hampton, Virginia
Sherrie Taylor Krist†
Vigyan Research Associates, Inc., Hampton, Virginia
and
W. Kyle Anderson‡
NASA Langley Research, Center, Hampton, Virginia

An upwind-biased finite-volume algorithm is applied to the low-speed laminar flow over a low-aspect-ratio delta wing from 0 to 40 deg angle of attack. The differencing is second-order accurate spatially and a multigrid algorithm is used to promote convergence to the steady state. The results compare well with the detailed experiments of Hummel and others for an Re_L of 0.95×10^6. The predicted maximum lift coefficient of 1.10 at 35 deg angle of attack agrees closely with the measured maximum lift of 1.06 at 33 deg. At 40 deg angle of attack, a bubble type of vortex breakdown is evident in the computations, extending from 0.6 of the root chord to just downstream of the trailing edge.

Nomenclature

$\mathcal{R}$ = aspect ratio
C = Sutherland's constant
c = speed of sound
e = total energy per unit volume
F,G,H = inviscid fluxes
H_v = viscous flux
J = transformation Jacobian, $= \partial(\xi,\eta,\zeta)/\partial(x,y,z)$
L = reference length, taken as a root chord
M = Mach number, $= \tilde{q}/\tilde{c}$; also, matrix for implicit time advancement
p = static pressure
Q = conservation variables
q = total velocity
$\dot{q}$ = heat flux terms
Re_L = Reynolds number, $= \tilde{\rho}_\infty \tilde{q}_\infty L/\tilde{\mu}_\infty$
T = temperature
t = time
U,V,W = contravariant velocities
u,v,w = Cartesian velocities in x,y, and z directions
x,y,z = Cartesian coordinates
α = angle of attack
γ = ratio of specific heats, $= 1.4$
δ = difference operator; also, flap deflection angle
λ = bulk viscosity coefficient
μ = molecular viscosity coefficient
ξ,η,ζ = general curvilinear coordinates
ρ = density
σ = Prandtl number
τ = shear stress tensor; also relative truncation error

Subscripts
x,y,z = differentiation with respect to x,y,z
∞ = conditions at freestream

Superscripts
$\hat{}$ = quantities in generalized coordinates
$\tilde{}$ = dimensional value

Introduction

THE experimental and computational simulation of the flow over a swept delta wing at high angle of attack is an area of intense research activity and is a focal point of the current interest in high angle of attack and vortical flows. These flows have applications to the blended wing-fuselage-strake configurations of modern, high-performance aircraft, which are tailored to take advantage of the highly nonlinear interacting vortices present at moderate to high angles of attack. The performance and stability characteristics of these designs are extremely difficult to predict a priori, and current design approaches rely extensively on the evolving experimental data base.

The prospects for developing analysis tools appropriate for such flows are brightened by the rapid and synergistic advances made in two areas: 1) computational fluid dynamics (CFD) and 2) nonintrusive experimental measurement techniques. The advances in CFD include the increased speed and memory of supercomputers, the improved accuracy and efficiency of computational algorithms, and the greatly increased geometric realism through incorporation of zonal mesh approaches. Since the solution times for three-dimensional computations are largely dictated by the number of grid points, the last item is extremely effective in reducing the overall computational time, because grid points can be concentrated in the areas where they are most needed.

Detailed experimental measurements of the flowfield are required to provide a definite validation of computational methods based on solutions to the Navier-Stokes equations. This is especially true for turbulent flow solutions to the Reynolds averaged equations. Laser Doppler velocimetry techniques, in combination with conventional measurement and innovative flow visualization approaches, can provide nonintrusive measurement in the sufficient detail and redundancy required.[1] There is a growing trend toward coordinated experimental and computational research with the objective of 1) benchmarking the current capabilities, as well as limita-

Presented as Paper 87-0207 at the AIAA 25th Aerospace Sciences Meeting, Reno, NV, Jan. 12-15, 1987; received Dec. 20, 1988; revision received June 15, 1989.

*Senior Research Scientist, Fluid Mechanics Division. Associate Fellow AIAA.
†Research Scientist.
‡Research Scientist, Fluid Mechanics Division. Member AIAA.

tions, of computational solutions and 2) providing the information required to improve the underlying physical and numerical models.

The flowfield over a low-aspect-ratio delta wing at angle of attack has been extensively studied both experimentally and computationally[2,3] and the overall physical structure of the flow is well understood. The characteristics of the flowfield are dominated by the two counter-rotating primary vortices that form over the wing because of separation at the leading edge. These vortices induce suction pressures over the upper surface of the wing and cause a nonlinear increase in lift over that attainable through attached flow. The adverse pressure gradients induced by the primary vortex can also lead to secondary and, sometimes, tertiary vortices. The maximum lift with increasing angle of attack is associated with the onset of vortex breakdown at the trailing edge. With further increases in angle of attack, the vortex breakdown point moves further forward on the wing until, at sufficiently high angle of attack, the flow is dominated by the periodic wake shedding encountered over bluff bodies.

Nonlinear, inviscid methods, which account for the leading-edge vortices and their interaction with the wing surfaces, have been developed and model the behavior of high Reynolds number, turbulent flow over sharp-edged wings extremely well.[2] To date, however, current methodology is restricted in that secondary separations and vortex breakdown effects are accounted for only empirically. The former is important for the accurate prediction of pressures, the latter for maximum lift. Computational methods based on the Navier-Stokes equations can predict both effects and are being rapidly advanced.

This paper presents initial computational results from a coordinated experimental and computational research program directed toward the documentation and validation of the low-speed flow over a highly swept delta wing. The computational method is a finite-volume algorithm for the compressible Navier-Stokes equations. Application of the method to a series of delta wings at supersonic freestream conditions is presented in Refs. 4 and 5. Results from the algorithm are presented below for the low-speed flow over an $\mathcal{R} = 1$ delta wing tested extensively by Hummel.[3] Computations are compared with experimental results from 0 to 40 deg angle of attack at a Reynolds number of 0.95×10^6. The effects of truncation error on the resulting accuracy of the solutions, as well as the effects of Mach number, are considered.

Governing Equations

The governing equations are the thin-layer approximations to the three-dimensional time-dependent compressible Navier-Stokes equations, written in generalized coordinates and conservation form as

$$\frac{\partial \hat{Q}}{\partial t} + \frac{\partial \hat{F}}{\partial \xi} + \frac{\partial \hat{G}}{\partial \eta} + \frac{\partial (\hat{H} - \hat{H}_v)}{\partial \zeta} = 0 \tag{1}$$

$$\hat{Q} = \frac{Q}{J} = \frac{1}{J}\begin{bmatrix} \rho \\ \rho u \\ \rho v \\ \rho w \\ e \end{bmatrix}, \qquad \hat{F} = \frac{1}{J}\begin{bmatrix} \rho U \\ \rho U u + \xi_x p \\ \rho U v + \xi_y p \\ \rho U w + \xi_z p \\ (e + p)U \end{bmatrix} \tag{2}$$

$$\hat{G} = \frac{1}{J}\begin{bmatrix} \rho V \\ \rho V u + \eta_x p \\ \rho V v + \eta_y p \\ \rho V w + \eta_z p \\ (e + p)V \end{bmatrix}, \qquad \hat{H} = \frac{1}{J}\begin{bmatrix} \rho W \\ \rho W u + \zeta_x p \\ \rho W v + \zeta_y p \\ \rho W w + \zeta_z p \\ (e + p)W \end{bmatrix} \tag{3}$$

$$\hat{H}_v = \frac{1}{J}\begin{bmatrix} 0 \\ \zeta_x \tau_{xx} + \zeta_y \tau_{xy} + \zeta_z \tau_{xz} \\ \zeta_x \tau_{xy} + \zeta_y \tau_{yy} + \zeta_z \tau_{yz} \\ \zeta_x \tau_{xz} + \zeta_y \tau_{yz} + \zeta_z \tau_{zz} \\ \zeta_x b_x + \zeta_y b_y + \zeta_z b_z \end{bmatrix} \tag{4}$$

$$U = \xi_x u + \xi_y v + \xi_z w \tag{5a}$$

$$V = \eta_x u + \eta_y v + \eta_z w \tag{5b}$$

$$W = \zeta_x u + \zeta_y v + \zeta_z w \tag{5c}$$

A general three-dimensional transformation between the Cartesian variables (x,y,z) and the generalized coordinates (ξ,η,ζ) is implied in Eq. (1), where ζ corresponds to the coordinate normal to the body surface. The vector Q represents density, momentum, and total energy per unit volume and p is the pressure defined from the equation of state for an ideal gas.

$$p = (\gamma - 1)[(e - \rho\,(u^2 + v^2 + w^2)/2)] \tag{6}$$

The equations are nondimensionalized in terms of the freestream density $\tilde{\rho}_\infty$ and sound speed $\tilde{c}_\infty$. The shear stress and heat flux terms are defined in tensor notation (summation convention implied) as

$$\tau_{x_i x_j} = \frac{M_\infty}{Re_L}\left[\mu\left(\frac{\partial u_i}{\partial x_j} + \frac{\partial u_j}{\partial x_i}\right) + \lambda \frac{\partial u_k}{\partial x_k}\delta_{ij}\right]$$

$$\dot{q}_{x_i} = -\left[\frac{M_\infty}{Re_L \sigma(\gamma - 1)}\right]\frac{\partial c^2}{\partial x_i}, \qquad b_{x_i} = u_j \tau_{x_i x_j} - \dot{q}_{x_i} \tag{7}$$

The chain rule is used to evaluate derivatives with respect to (x,y,z) in terms of (ξ,η,ζ). Consistent with the thin-layer assumption, only those derivatives in the direction normal to the wall (ζ) are retained in the shear stress and heat flux terms. Equation (1) is closed by Stokes hypothesis for bulk viscosity $(\lambda + 2\mu/3 = 0)$ and Sutherland's law for molecular viscosity. All calculations presented are for laminar flow.

Computational Algorithm

Spatial Differencing

Second-order-accurate upwind-biased spatial differencing, as described below and elsewhere[4-6] is used for all of the results presented below. The generalized fluxes $\hat{F}$, $\hat{G}$, $\hat{H}$, representing pressure and convection terms are upwind differenced with a flux-vector-splitting method, i.e., split into forward and backward contributions and differenced accordingly. For example, the flux difference in the ξ direction is

$$\delta_\xi \hat{F} = \delta_\xi^- \hat{F}^+ + \delta_\xi^+ \hat{F}^- \tag{8}$$

where δ_ξ^- and δ_ξ^+ denote general backward and forward divided difference operators, respectively, in the ξ direction. The flux vector in three-dimensional generalized coordinates is split according to the scheme of Van Leer. The flux $\hat{F}$, as an example, is split according to the contravariant Mach number in the ξ direction, defined as $M_\xi = \bar{u}/c$, where $\bar{u} = U/|\text{grad}\xi|$. For supersonic flow, $|M_\xi| \geq 1$

$$\hat{F}^+ = \hat{F}, \qquad \hat{F}^- = 0, \qquad M_\xi \geq +1 \tag{9a}$$

$$\hat{F}^- = \hat{F}, \qquad F^+ = 0, \qquad M_\xi \leq -1 \tag{9b}$$

and for subsonic flow, $|M\hat{\xi}|<1$

$$\hat{F}^{\pm}=\frac{|\text{grad}\xi|}{J}\begin{bmatrix} f^{\pm}_{\text{mass}} \\ f^{\pm}_{\text{mass}}\,[\hat{k}_x(-\bar{u}\pm 2c)/\gamma+u] \\ f^{\pm}_{\text{mass}}\,[\hat{k}_y(-\bar{u}\pm 2c)/\gamma+v] \\ f^{\pm}_{\text{mass}}\,[\hat{k}_x(-\bar{u}\pm 2c)/\gamma+w] \\ f^{\pm}_{\text{energy}} \end{bmatrix} \tag{10}$$

where

$$f^{\pm}_{\text{mass}}=+\rho c(M_\xi\pm 1)^2/4$$

$$f^{\pm}_{\text{energy}}=f^{\pm}_{\text{mass}}\left[\frac{(1-\gamma)\bar{u}^2\pm 2(\gamma-1)\bar{u}c+2c^2}{(\gamma^2-1)}+\frac{(u^2+v^2+w^2)}{2}\right]$$

The equations are written in generalized coordinates but are solved with a finite-volume approach, where the metric terms are evaluated geometrically. The surface area of the cell interface in the ξ direction is $|\text{grad}\xi|/J$, the cell volume is $1/J$, and

$$(\hat{k}_x,\hat{k}_y,\hat{k}_z)=(\xi_x,\xi_y,\xi_z)/|\text{grad}\xi| \tag{11}$$

are the direction cosines of the cell interfaces in the ξ direction, for example.

The split-flux differences are implemented as a flux balance across the ith cell holding spatial indices j and k constant as (for $\Delta\xi=\Delta\eta=\Delta\zeta=1$)

$$\delta_\xi^-\hat{F}_i^+ + \delta_\xi^+\hat{F}_i^- = [\hat{F}^+(Q^-)+\hat{F}^-(Q^+)]_{i+1/2} - [\hat{F}^+(Q^-)+\hat{F}^-(Q^+)]_{i-1/2} \tag{12}$$

The notation $\hat{F}^+(Q^-)_{i+1/2}$ denotes a forward flux evaluated using the metric terms at the cell interface $(i+1/2)$, and state variables obtained by fully upwind second-order interpolation of cell-centered variables

$$Q^-_{i+1/2}=(3/2)Q_i-(1/2)Q_{i-1} \tag{13a}$$

$$Q^+_{i+1/2}=(3/2)Q_{i+1}-(1/2)Q_{i+2} \tag{13b}$$

Differencing for the diffusion terms representing shear stress and heat transfer effects corresponds to second-order central differences, in which second derivatives are treated as differences across cell interfaces of first derivative terms, as below, holding spatial indices i and j constant.

$$\delta_\zeta\hat{H}_{v_k}=\hat{H}_{v_{k+1/2}}-\hat{H}_{v_{k-1/2}} \tag{14}$$

The term $H_{v_{k+1/2}}$ is defined as

$$\hat{H}_v=\frac{M_\infty\mu}{Re_L J}\begin{bmatrix} 0 \\ \phi_1 u_\zeta+\zeta_x\phi_2 \\ \phi_1 v_\zeta+\zeta_y\phi_2 \\ \phi_1 w_\zeta+\zeta_z\phi_2 \\ \phi_1\left[\left(\frac{q^2}{2}\right)_\zeta+\frac{1}{\sigma(\gamma-1)}(c^2)_\zeta\right]+W\phi_2 \end{bmatrix} \tag{15}$$

where

$$\phi_1=\zeta_x^2+\zeta_y^2+\zeta_z^2 \qquad \phi_2=(\zeta_x u_\zeta+\zeta_y v_\zeta+\zeta_z w_\zeta)/3$$

and $\delta_\zeta u_{k+1/2}=u_{k+1}-\mu_k$. Implemented in a finite-volume-approach, the preceding formula requires an approximation to the volume at the cell interface $(1/J)_{k+1/2}$, which is calculated by averaging the neighboring values.

Time Differencing

The linearized, backward-time approximation in delta form for the three-dimensional equations is given as

$$\left[\frac{I}{J\Delta t}+\delta_\xi\frac{\partial\hat{F}}{\partial Q}+\delta_\eta\frac{\partial\hat{G}}{\partial Q}+\delta_\zeta\left(\frac{\partial\hat{H}-\partial\hat{H}_v}{\partial Q}\right)\right]\Delta Q=-L(Q^n) \tag{16}$$

where $L(Q^n)$ is the discrete representation of the spatial derivative terms in Eq. (1), evaluated at time level n. Equation (16) is spatially factored and solved as a series of sweeps through the mesh.

$$\left[\frac{I}{J\Delta t}+\delta_\eta\frac{\partial\hat{G}}{\partial Q}\right]\Delta Q^*=-L(Q^n) \tag{17a}$$

$$\left[\frac{I}{J\Delta t}+\delta_\zeta\left(\frac{\partial\hat{H}-\partial H_v}{\partial Q}\right)\right]\Delta Q^{**}=\left(\frac{I}{J\Delta t}\right)\Delta Q^* \tag{17b}$$

$$\left[\frac{I}{J\Delta t}+\delta_\xi\frac{\partial\hat{F}}{\partial Q}\right]\Delta Q=\left(\frac{I}{J\Delta t}\right)\Delta Q^{**} \tag{17c}$$

$$Q^{n+1}=Q^n+\Delta Q \tag{17d}$$

The algorithm is written in delta form so that the steady-state solutions are independent of the time step Δt.

The implicit spatial derivatives of the convective and pressure terms are first-order accurate, leading to block tridiagonal inversions for each sweep. The algorithm is conditionally stable and optimal convergence is obtained with a spatially varying time step corresponding to a Courant number on the order of 10. The operations are completely vectorizable in η but are vectorized over the other two directions.

Convergence Acceleration

The full approximation scheme (FAS) multigrid algorithm, developed and applied to inviscid three-dimensional flows in Refs. 7 and 8, is used to accelerate convergence to the steady state. A sequence of grids G_0,G_1,G_N is defined, where G_N denotes the finest grid and coarser grids are formed by successively deleting every other line in all three coordinate directions. The fine grid serves to damp the high-frequency errors; the coarser grids damp the low-frequency errors. The coarse grids are solved with a forcing function on the right-hand side, arising from restricting the residual from the finer meshes. The forcing function is the relative truncation error between the grids, such that the solution on the coarser meshes are driven by the fine grid residual. The resulting scheme on mesh G_i is given as

$$M_i\Delta Q_i^c=-[L_i(Q_i^c)-\tau_i]\equiv -R_i \tag{18}$$

where Q_i^c is the current approximation to the solution on mesh G_i, M_i the spatially-factored implicit matrix, and τ_i the relative truncation error, where τ_N is defined to be zero. The relative truncation error is calculated as

$$\tau_i=L_i(I^i_{i+1}Q^c_{i+1})-\tilde{I}^i_{i+1}R_{i+1} \tag{19}$$

The operator I^i_{i+1} is a volume-weighted restriction operator that transfers values on the finer grid to the coarser grid

$$I^i_{i+1}Q_{i+1}=\Sigma\left(\frac{Q_{i+1}}{J_{i+1}}\right)\Big/\Sigma\left(\frac{1}{J_{i+1}}\right) \tag{20}$$

where the summation is taken over the eight finer grid cells that make up the coarser grid. The restriction operator $\tilde{I}^i_{i+1}$

for the residual is

$$\tilde{I}^{i}_{i+1}R_{i+1} = \sum R_{i+1} \tag{21}$$

where the summation is as above. The corrections on the coarse meshes

$$V_i = \boldsymbol{Q}^c_i - I^i_{i+1}\boldsymbol{Q}^c_{i+1} \tag{22}$$

are used to update the finer mesh

$$\boldsymbol{Q}^c_i \leftarrow \boldsymbol{Q}^c_i + I^i_{i-1}V_{i-1} \tag{23}$$

where the operator I^i_{i-1} corresponds to trilinear interpolation.

A fixed cycling strategy (W cycle) is used for the results presented, as illustrated in Fig. 1 for the typical case of four grid levels. It was found necessary to smooth the solutions on each grid through four to five steps of the operator M before switching to the next mesh. This is in contrast to the results obtained for solutions to the Euler equations, where a single step was sufficient, and is attributed to the poorer damping characteristics of the algorithm on highly stretched meshes. Convergence to the steady state was determined when the lift coefficient demonstrated less than a 2% change over 100 iterations, which corresponded to a four order-of-magnitude reduction in the residual. The multigrid algorithm proved effective in eliminating a large amplitude damped oscillation in lift encountered with the single grid algorithm. Approximately 2.5 h on the NASA Langley VPS-32 (CYBER 205) computer are required to obtain a converged solution for a grid of 550,000 points, based on 400 fine grid iterations and a computational rate of 40 μs/grid point/iteration, using 32-bit arithmetic operations. In all cases, solutions from either a coarser mesh or a nearby angle of attack were used to initialize the computations on a given mesh.

Grid Topology and Boundary Conditions

A representative grid topology is shown in Fig. 2 for the $\mathcal{R}=1$ wing, corresponding to a grid of $33\times33\times33$ points in the $\eta-$, $\zeta-$, and $\xi-$ coordinate directions, respectively, where η is the circumferential coordinate and ξ is the axial coordinate. The grid extends approximately one root chord upstream and downstream of the wing and two root chords circumferentially away from the centerline. Along the far-field upstream and circumferential boundaries, a quasi-one-dimensional characteristic analysis is used to determine the boundary data, assuming freestream conditions exterior to the boundary. Along the downstream boundary, first-order extrapolation of the conserved variables is used. There are undoubtedly some effects on the solution because of the finite extent of the boundaries, but the effects have not been quantified as yet.

The cross-sectional grids are generated with a sheared conformal transformation, and are clustered near the surface to resolve viscous effects, as shown in Fig. 3. The minimum spacing normal to the wing surface on the finest grid varies from 0.1×10^{-4} at the apex to 0.5×10^{-4} at the trailing edge, referenced to a distance of unity for the root chord. The upper surface of the wing is flat with sharp leading edges; the lower surface of the grid is sheared to correspond to the geometry tested by Hummel. At the wall, the velocity is set to zero, the temperature is set to the freestream total temperature, and pressure is determined from a zero normal pressure gradient assumption. Symmetry conditions are used along the vertical plane of symmetry. The cross-sectional grids are clustered streamwise near the apex and trailing edge. The region downstream of the trailing edge is also sheared vertically, so that the far downstream boundary is tangent to the angle of attack.

Results

The experimental measurements of Hummel[9] were carried out on a sharp-edge delta wing of $\mathcal{R}=1$, which corresponds to a sweep angle of 75.9638 deg. The upper surface of the wing was flat and the cross section was triangular ahead of $x/L=0.9$, with maximum thickness $0.021L$. The cross sections downstream of $x/L=0.9$ were trapezoidal (Fig. 3), such that the trailing edge was sharp. This leads to a mean camber surface that causes a slight negative lift at 0 deg angle of attack. The low-speed experiments ($M_\infty\approx0.1$) were performed in a 1.3-m open jet wind tunnel of circular cross section and included measurements of forces, surface pressures, surface oil flows, and flowfield surveys at laminar and turbulent conditions.

Based on a number of experimental investigations, the flowfield above the wing in a transverse cross section is sketched in Fig. 4. The flow separates at the leading edge and rolls into the primary vortex above the wing. The primary vortex induces an adverse pressure gradient along the flow proceeding outward from the primary attachment line, causing a secondary separation-induced vortex. The secondary vortex can in turn lead to a tertiary vortex underneath and inboard of the secondary vortex. The overall features of the process remain the same for laminar or turbulent flows, the influence of turbulence being to delay the secondary separation to a more outboard position and generally to eliminate any tertiary separation.

The surface flow computed with the present method at $M_\infty=0.3$ is compared with the oil flow results of Hummel[9] in Fig. 5 at an angle of attack of 20.5 deg. There is excellent agreement of the secondary and tertiary separation lines. At this angle of attack, the primary attachment occurs on the centerline. The secondary and tertiary attachment lines shown on the left were not reported by Hummel but were sketched onto his results to reflect the flow topology in Fig. 4. The location of the attachment lines are difficult to determine experimentally, especially the secondary attachment, since it occurs so near the leading edge. The experimental results indicate an outboard movement of the secondary separation line near the trailing edge that is associated with the onset of

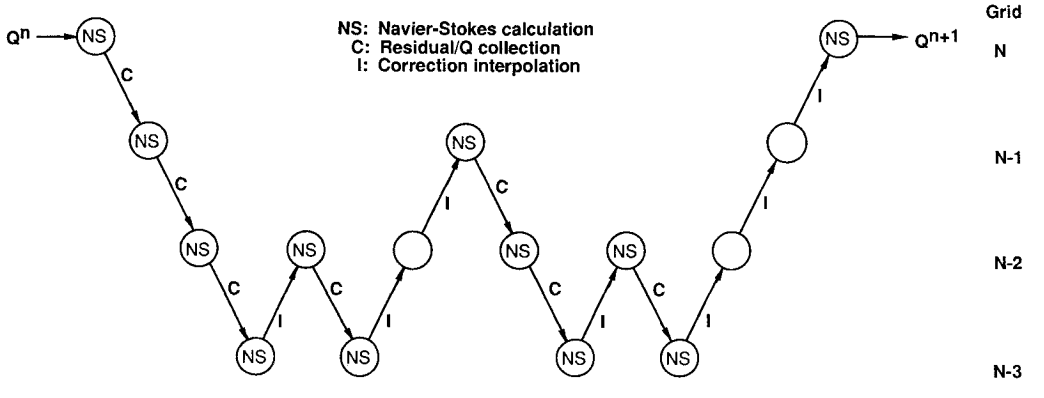

Fig. 1 Multigrid W cycle.

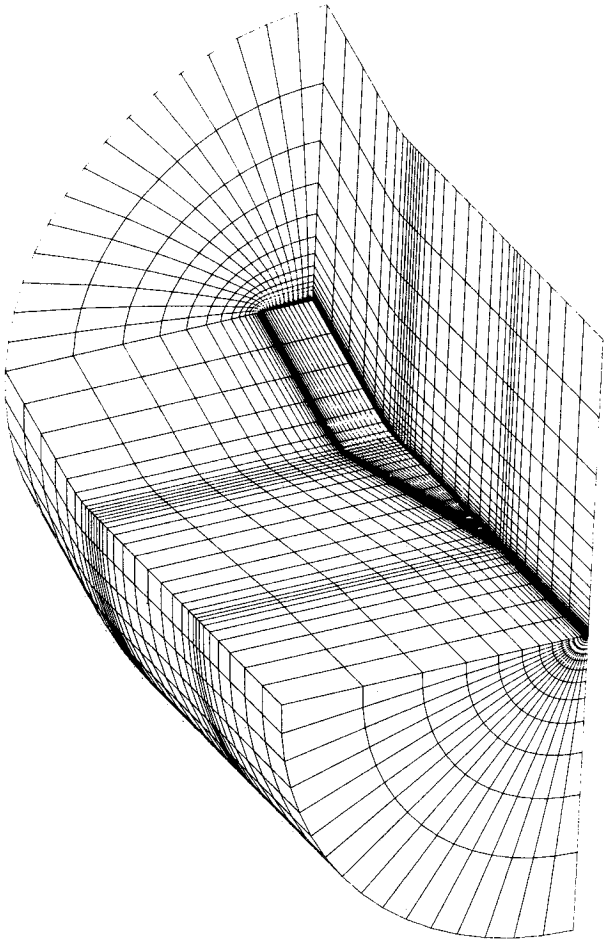

Fig. 2 Three-dimensional grid for delta wing.

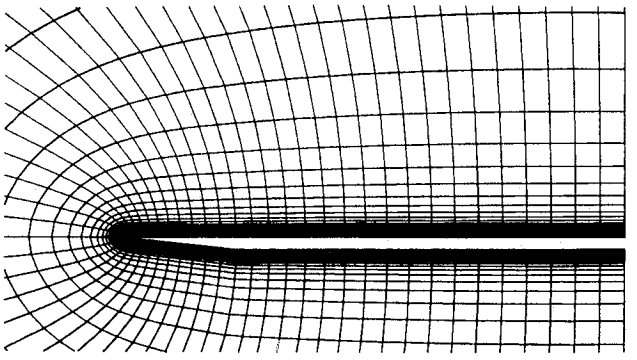

Fig. 3 Cross-sectional grid for delta wing.

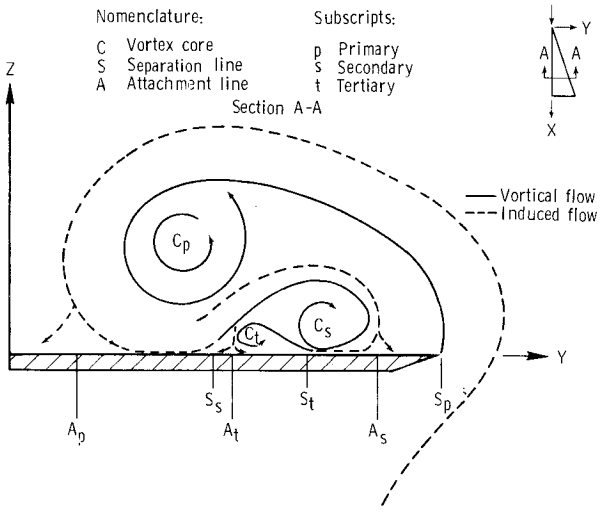

Fig. 4 Schematic of crossflow over delta wing.

turbulent flow. The transition location is in good agreement with the experimental results for a 75 deg swept delta wing reported recently by Kjelgaard et al.[10] and Carcaillet et al.[11] The laminar computations, on the other hand, indicate a small region of reverse flow near the trailing edge in the vicinity of the secondary separation line. Further inspection of the computations indicates that the separation has only a very limited extent in the normal direction.

A perspective view of the total pressure contours computed with the present method (Fig. 6) evidences clearly the streamwise development of the primary and secondary vortices over the wing. The tertiary vortex cannot be seen in the contours shown, since it is extremely small and lies very near the surface. The primary vortex core locations agree closely with experimental results.[10] The primary vortex field exhibits a nearly conical structure, as seen in the present results, and also experimentally.[11] It is known from experiment that the total lift coefficient and primary vortex positions remain nearly the same for laminar or turbulent flows. The influence of Reynolds number can be attributed to the behavior of the secondary vortex field. A comparison made in Fig. 7 at an angle of attack of 20.5 deg shows good agreement for the overall shape of the primary vortex from the present computations with the smoke visualization results of Kjelgaard et al.[10] for a 75 deg swept delta wing.

A comparison of the surface pressure with the experiment of Hummel is shown in Fig. 8 at a series of longitudinal stations. The computations shown, as well as those just discussed, correspond to a freestream Mach number 0.30 on a baseline $129 \times 65 \times 65$ grid. At the forward stations, the overall level of the minimum pressure coefficient under the primary and secondary vortices agrees closely with the experimental results. At the $x/L = 0.9$ station, the pressure under the primary vortex is overpredicted and no evidence of the tertiary vortex is evident in the experimental results. Both effects are consistent with the onset of turbulent flow in the experiment near the trailing edge, which is not presently being modeled. The predicted pressures are slightly lower than the experimental pressures along the upper surface centerline, especially near the apex. The lower surface pressures agree closely with the experiment, except at $x/L = 0.9$. At this station, the predicted

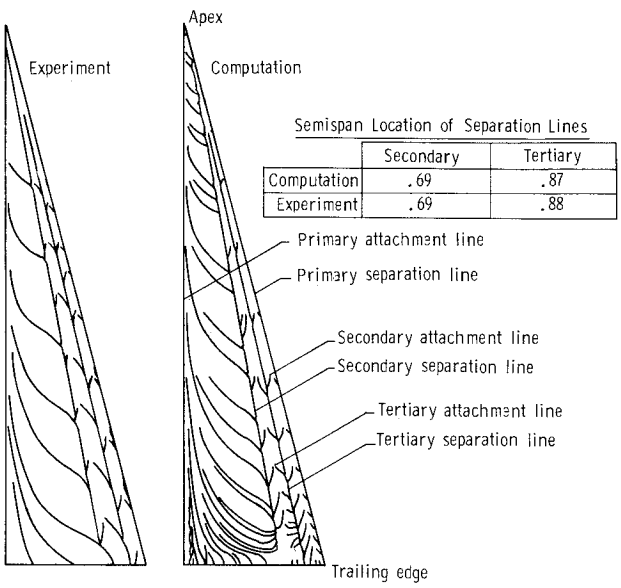

Fig. 5 Surface flow visualizations; $\alpha = 20.5$ deg, $Re_L = 0.95 \times 10^6$.

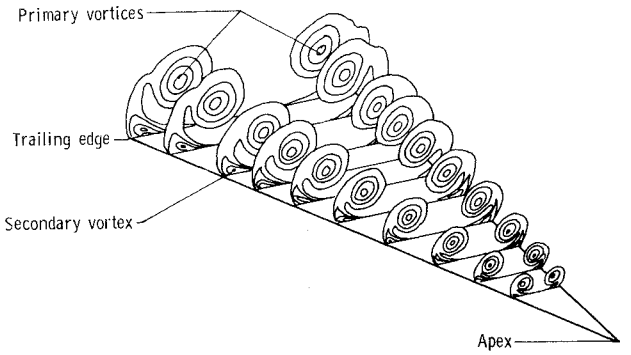

Fig. 6 Total pressure contours; $\alpha = 20.5$ deg, $Re_L = 0.95 \times 10^6$.

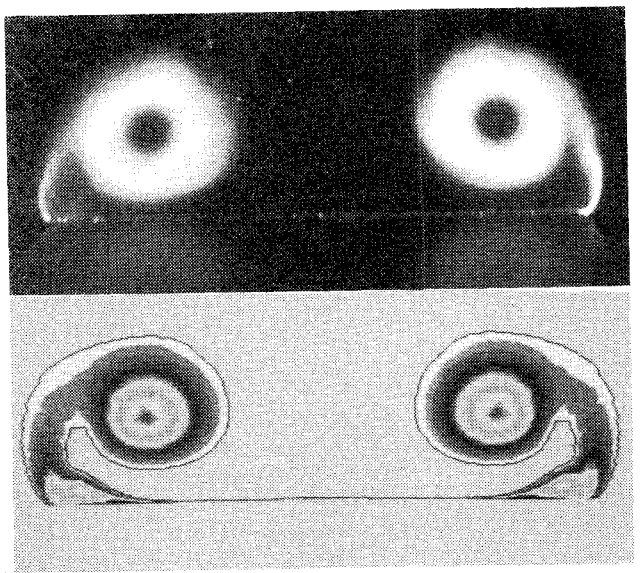

Fig. 7 Comparison of computed total pressure contours with smoke visualization of Kjelgaard et al.[10]

pressures show the influence of the expansion over the negative camber on the wing undersurface, whereas no such effect is seen in the experimental data. In fact, the lower surface computations for a completely flat wing agree very closely with the experimental results. The reason for the disagreement is not known, although it can be surmised that the disagreement is because of interference caused by the presence of the pressure tubing that exits from the model in the lower surface trailing-edge region.

The effects of grid refinement on the spanwise pressure distribution are shown in Fig. 9. The stations nearest the apex are the stations most sensitive to grid refinement, and successively coarser grid variations from two grids of approximately 125,000 ($65 \times 65 \times 33$) and 550,000 ($129 \times 129 \times 33$) points are shown at $x/L = 0.3$. Reasonable results are obtained with a grid of 125,000 points, although the accuracy deteriorates rapidly for fewer grid points. Results from Fig. 8 for the baseline computational grid ($129 \times 65 \times 65$) are in close agreement with the finest grid results in Fig. 9. Although not shown, computations were also made with a grid of $97 \times 97 \times 33$ points, for which the pressure distribution is nearly the same as the baseline grid. Note, however, that the pressure on the upper surface centerline, which is lower than the experiment, is not affected by grid refinement. Near the leading edge, the results indicate a spurious pressure decrease/increase on the upper/lower surface that diminishes in both magnitude and extent with grid refinement. The sensitivity of the calculation to the grid is in agreement with the previous results of Fujii and Kutler,[12,13] who concluded quantitative predictions are not possible without a grid substantially finer

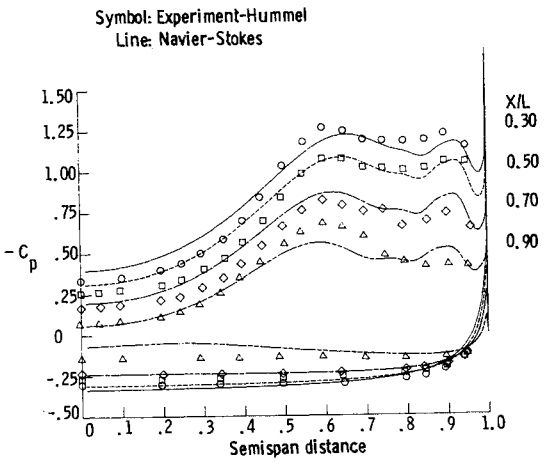

Fig. 8 Surface pressure comparison between experiment and present computations; $\alpha = 20.5$ deg, $Re_L = 0.95 \times 10^6$.

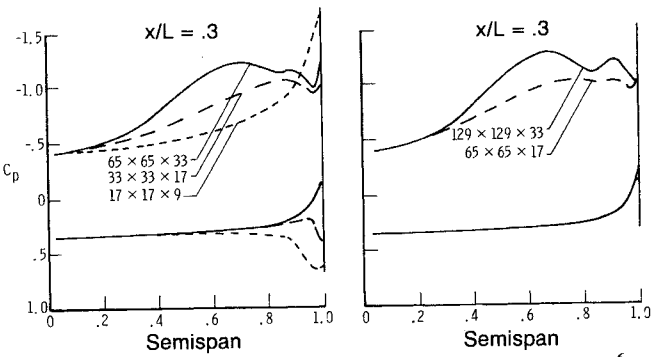

Fig. 9 Effect of grid refinement, $\alpha = 20.5$ deg, $Re_L = 0.95 \times 10^6$.

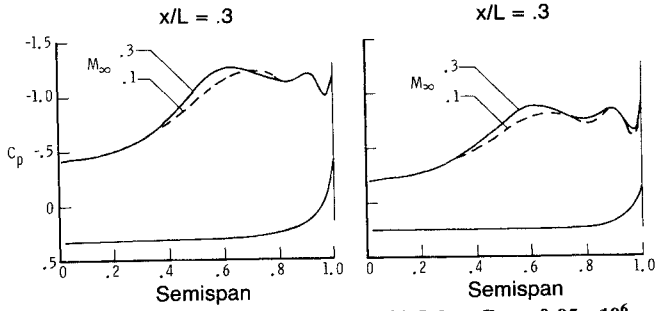

Fig. 10 Effect of Mach number, $\alpha = 20.5$ deg, $Re_L = 0.95 \times 10^6$.

than 60,000 points. Note that the grid convergence results presented here are restricted to the variation of properties on the surface, near which the grid is much more highly clustered than, say, the vortex core region. Embedded zonal grids can be efficiently used to increase the resolution at locations away from the surface.

The effect of Mach number on the spanwise pressure distribution at two longitudinal stations is shown in Fig. 10. The effect of increasing the Mach number is to decrease slightly the pressure coefficient under the primary vortex and move the peak inboard at both stations. The pressures elsewhere change only slightly with variations in the Mach number. The trends with Mach number are the same as those obtained by Fujii and Kutler[13] previously.

The lift curve variation with angle of attack is shown in Fig. 11; the computed points were obtained at five-degree increments in angle of attack. The negative lift due to camber at 0 deg angle of attack is well predicted, as is the nonlinear variation of lift through the angle of attack range up to 30 deg. The

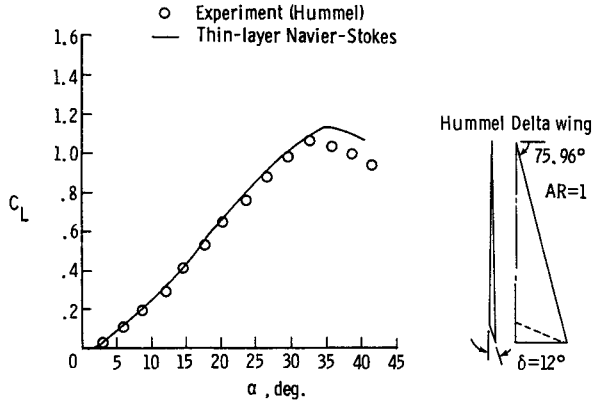

Fig. 11 Lift curve variation with angle of attack, $Re_L = 0.95 \times 10^6$.

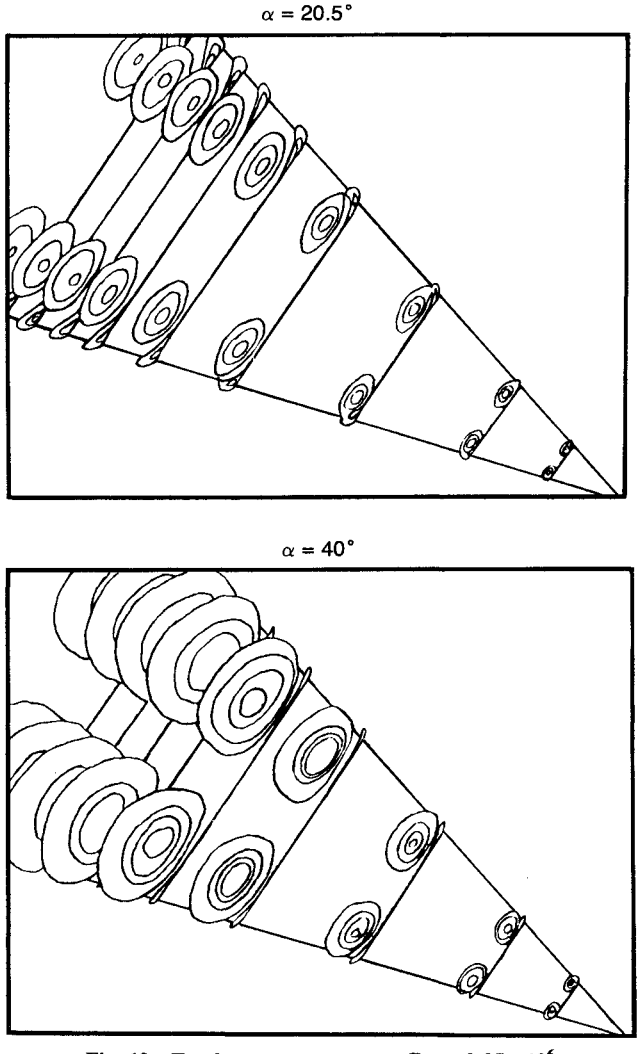

Fig. 12 Total pressure contours; $Re_L = 0.95 \times 10^6$.

maximum lift coefficient of 1.06 in the experiment occurs at 33 deg angle of attack, which is coincident with the onset of vortex breakdown at the trailing edge of the model. The present results predict a maximum lift of 1.10 at 35 deg, in reasonably close agreement with the experiment.

In Fig. 12, perspective views of the total pressure contours at $\alpha = 20.5$ and 40 deg are compared. At the higher angle of attack, the vortices are much larger, nearly equal to the semispan in diameter. Also, the contours indicate that the region of maximum total pressure loss increases rapidly downstream of $x/L = 0.5$. In Fig. 13, a perspective from the same viewpoint of streamwise velocity contours for the $\alpha = 40$ deg case is shown. The maximum streamwise velocities ($u/u_\infty \geq 1.2$) occur in the acceleration of the flow around the leading edge in the apex region. A pocket of reverse streamwise velocity ($u/u_\infty \leq -0.1$) occurs in the vortex core region upstream of the trailing-edge region. The results are indicative of the "bubble" type of vortex breakdown,[14] in which the axial velocity stagnates on the center of the vortex axis ahead of an abrupt expansion of the streamline over a bubble of recirculating fluid. Particle traces (not shown here) above the wing at $\alpha = 40$ deg indicate that the region of recirculating flow extends from approximately $x/L = 0.6$ to just downstream of the trailing edge. Payne et al.[15] report both "bubble" and "spiral" types of vortex breakdown occurred periodically with time over the upper surface of a 75 deg swept wing at $Re_L = 0.42 \times 10^6$, with a mean axial location of $x/L = 0.4$ at 40 deg angle of attack.

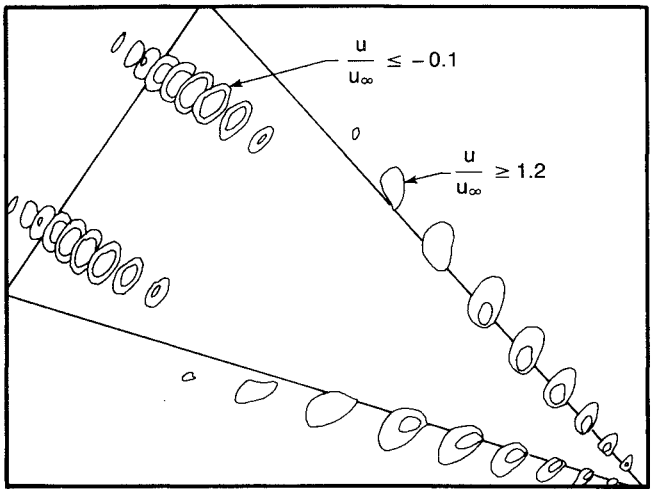

Fig. 13 Streamwise velocity contours; $\alpha = 40$ deg, $Re_L = 0.95 \times 10^6$.

In vortex tube experiments simulating the vortex breakdown process, the region of recirculating fluid in the vortex bubble is followed by a transition to turbulent flow. The transitional processes cannot be predicted with the present method, but it can be speculated that the turbulent field downstream of the burst vortex might not be a critical parameter in determining the onset of the breakdown region. Very little quantitative experimental data exit in the angle of attack ranges leading to vortex breakdown over delta wings.

Concluding Remarks

An upwind-biased finite-volume algorithm has been applied to the low-speed flow over a low aspect-ratio delta wing from 0 to 40 deg angle to attack. The differencing is second-order accurate spatially and a multigrid algorithm is used to promote convergence to the steady state. The results compare well with the detailed experiments of Hummel and others for a Re_L of 0.95×10^6. The predicted maximum lift coefficient of 1.10 at 35 deg angle of attack agrees closely with the measured maximum lift of 1.06 at 33 deg. At 40 deg angle of attack, a bubble type of vortex breakdown is evident in the computations, extending from 0.6 of the root chord to just downstream of the trailing edge.

For higher Reynolds numbers, some account of the turbulent shear stresses needs to be implemented; the effect of turbulent flow is already evident in the present comparisons in the vicinity of the trailing edge. Experimental results detailing the streamwise location of the transitional zones are available,[10,11] including the variation with Reynolds number and angle of attack. However, more extensive and detailed experimental results are required in order to allow a complete assessment of the present prediction techniques, especially for turbulent flows and in the angle of attack regions leading to vortex breakdown.

References

[1]Sellers, W. L., III and Kjelgaard, S. O., "The Basic Aerodynamics Research Tunnel—A Facility Dedicated to Code Validation," AIAA Paper 88-1997, 1988.

[2]Luckring, J. M. and Thomas, J. L., "Separation Induced Vortex Flow Effects—Some Capabilities and Limitations," First National Aerospace Plane Technology Symposium, May 20–22, 1986.

[3]Hummel, D., "On the Vortex Formation Over a Slender Wing at Large Angles of Incidence," AGARD CP-247, Paper No. 15, Feb. 1983.

[4]Thomas, J. L. and Newsome, R. W., "Navier-Stokes Computations of Lee-Side Flows Over Delta Wings," AIAA Paper 86-1049, May 1986.

[5]Newsome, R. and Thomas, J. L., "Computation of Leading-Edge Vortex Flows," NASA CP 2416, Oct. 1985.

[6]Walters, R. W., Thomas, J. L., and Van Leer, B., "An Implicit Flux-Split Algorithm for the Compressible Euler and Navier-Stokes Equations," *Tenth International Conference on Numerical Methods in Fluid Dynamics*, June 1986.

[7]Anderson, W. K., Thomas, J. L., and Whitfield, D. L., "Multigrid Acceleration of the Flux Split Euler Equations," AIAA Paper 86-0274, Jan. 1986.

[8]Anderson, W. K., "Implicit Multigrid Algorithms of the Three-Dimensional Flux Split Euler Equations," Ph.D. Dissertation, Mississippi State Univ., MS, Aug. 1986.

[9]Hummel, D., "Study of the Flow Around Sharp-Edged Slender Delta Wings with Large Angles of Attack," NASA TTF-15, Vol. 107, Sept. 1973.

[10]Kjelgaard, S. O., Sellers, W. L., III, and Weston, R. P., "The Flowfield Over a 75 Degree-Swept Delta Wing at 20.5 Degrees Angle of Attack," AIAA Paper 86-1775CP, June 1986.

[11]Carcaillet, R., Manie, F., Pagan, D., and Solignac, J. L., "Leading Edge Vortex Flow Over a 75 Degree-Swept Delta Wing—Experimental and Computational Results," International Council of the Aeronautical Sciences, Paper ICAS-86-1.5.1, Sept. 1986.

[12]Fujii, K. and Kutler, P., "Numerical Simulation of the Viscous Flow Over Three-Dimensional Complicated Geometries," AIAA Paper 84-1550, June 1984.

[13]Fujii, K. and Kutler, P., "Numerical Simulation of the Leading Edge Separation Vortex for a Wing and Strake-Wing Configuration," AIAA Paper 83-1908CP, July 1983.

[14]Faler, J. H. and Leibovich, S., "Disrupted States of Vortex Flow and Vortex Breakdown," *Physics of Fluids*, Vol. 20, No. 9, Sept. 1977, pp. 1385–1400.

[15]Payne, F. M., Ng, T. T., Nelson, R. C., and Schiff, L. B., "Visualization and Flow Surveys of the Leading Edge Vortex Structure on Delta Wing Planforms," AIAA Paper 86-0330, Jan. 1986.